An Empirical Proxy for the Second Integral of Motion in Rotating Barred or Tri-axial Potentials

Yu-Jing Qin[1] and Juntai Shen[2,3,4]

[1] Steward Observatory, University of Arizona, 933 N. Cherry Ave., Tucson, AZ 85721, USA

[2] Department of Astronomy, School of Physics and Astronomy, Shanghai Jiao Tong University, 800 Dongchuan Rd., Shanghai 200240, People's Republic of China
jtshen@sjtu.edu.cn

[3] Key Laboratory for Particle Astrophysics and Cosmology (MOE)/Shanghai Key Laboratory for Particle Physics and Cosmology, Shanghai 200240, People's Republic of China

[4] Shanghai Astronomical Observatory, Chinese Academy of Sciences, 80 Nandan Rd., Shanghai 200030, People's Republic of China

Abstract

We identify an effective proxy for the analytically unknown second integral of motion (I_2) for rotating barred or tri-axial potentials. Planar orbits of a given energy follow a tight sequence in the space of the time-averaged angular momentum and its amplitude of fluctuation. The sequence monotonically traces the main orbital families in the Poincaré map, even in the presence of resonant and chaotic orbits. This behavior allows us to define the calibrated angular momentum, the average angular momentum ($\overline{L_z}$) normalized by the amplitude of its fluctuation (σ_{L_z}), as a numerical proxy for I_2. It also implies that the amplitude of fluctuation in L_z, previously underappreciated, contains valuable information. This new proxy allows one to classify orbital families easily and accurately, even for real orbits in N-body simulations of barred galaxies. It is a good diagnostic tool of dynamical systems, and may facilitate the construction of equilibrium models.

Unified Astronomy Thesaurus concepts: Galaxy dynamics (591); Orbits (1184); Barred spiral galaxies (136)

1. Introduction

An integral of motion (IoM) $I(x, v)$ is any time-independent function of the phase-space coordinates that is strictly conserved along an orbit. The isolating IoMs, unlike the nonisolating ones, are of great importance as they reduce the dimensionality of the phase-space nontrivially and impose fundamental constraints on a dynamical system (Binney & Tremaine 2008).

Isolating IoMs can be categorized into classical IoMs and nonclassical IoMs. Classical IoMs have known analytical expressions, while nonclassical IoMs do not. Examples of classical IoMs include the Hamiltonian in any time-independent potential, all components of the angular momentum vector in spherical potentials, and the axial component of angular momentum (L_z) for axisymmetric potentials. They reflect the symmetries and conservation laws of the system via Noether's theorem. The higher degree of symmetry in Keplerian and harmonic potentials allows even more isolating IoMs. For separable potentials in a certain coordinate system, the equation of motion can be decomposed to decoupled motions in each direction, and the classical IoMs may be obtained (e.g., Stäckel potentials).

Nonclassical IoMs, on the contrary, do not have known analytic expressions of phase-space coordinates x and v. Their existence is inferred by the fact that a numerically integrated orbit at a given energy is confined to a closed invariant curve (e.g., Henon & Heiles 1964) in the Poincaré map, also known as the surfaces of section (SoS). Realistic potentials often contain such nonclassical integrals, which are usually dubbed as the second (I_2) or the third integral (I_3), since they are in addition to the classical integrals like H and/or L_z. In a Hamiltonian system with n degrees of freedom, regular orbits that admit n isolating IoMs appear as closed[5] invariant curves

in the Poincaré map, as they are confined to n-D toroidal surfaces (orbital tori). Conversely, chaotic orbits have fewer than n isolating IoMs, so they are diffusive in the Poincaré map. The nonreducible frequency components of an orbit also indicate the number of isolating IoMs, where each fundamental frequency corresponds to an action variable (J) in action-angle coordinates (Binney & Spergel 1982, 1984; Laskar 1993; Valluri & Merritt 1998).

For a steady-state system, the distribution function (DF) can be parameterized using only the isolating IoMs (Lynden-Bell 1962). Given their elegant properties and fundamental roles in classical mechanics, IoMs are extensively used as diagnostic tools for dynamical systems.

Here we focus on the nonclassical IoMs in rotating barred potentials, which are common and useful in astronomy. Nearly two-thirds of disk galaxies in the universe contain a central elongated bar structure (e.g., Menéndez-Delmestre et al. 2007; Masters et al. 2011), including our own Milky Way (e.g., Binney et al. 1991; Blitz & Spergel 1991). Bars are not static structures: in a disk galaxy they rotate rapidly. Tri-axial elliptical galaxies may also have some figure rotation similar to barred galaxies. The orbital structure in a rotating barred potential has been extensively studied (Contopoulos & Grosbol 1989; Sellwood & Wilkinson 1993; Patsis et al. 2002; Skokos et al. 2002; Binney & Tremaine 2008); the common regular orbital families include prograde x_1 orbits, retrograde x_4 orbits, and x_2/x_3 orbits if an inner Lindblad resonance (ILR) exists.

In a rotating nonaxisymmetric potential, the only classical IoM is the Jacobi integral ($H_J = H - \Omega \cdot L$), which is the Hamiltonian in the rotating frame. Note that the angular momentum is not an IoM in either the inertial or bar-corotating frame. The Poincaré map for 2D planar orbits in a rotating barred potential shows clear nested invariant curves, implying that at least some orbits are confined to orbital tori by an additional IoM (I_2) besides H_J.

---

[5] However, invariant curves may become nonclosed, splitting into two disconnected line segments, under certain conditions in a rotating frame (Binney et al. 1985; Xia & Shen 2021). Thus the defining characteristic of regular orbits is quasi-periodicity.

Our main motivation is to identify an empirical proxy for the analytically unknown I_2 in a rotating barred potential, which can immediately facilitate the classification of orbits of a given energy. Angular momentum is time-varying in a rotating barred potential, but interestingly we can indeed find such a proxy in the angular momentum space. The amplitude of fluctuation in L_z may also contain valuable information on orbits but was not given enough attention in the past. With simple 2D orbits of test particles, we demonstrate that the calibrated angular momentum (CAM), the average angular momentum ($\overline{L_z}$) normalized by the amplitude of its fluctuation (σ_{L_z}), is an excellent numerical proxy for I_2.

2. Potential and Orbital Integration

Without loss of generality, we adopt a rotating logarithmic bar potential of the following form (Equation (3.103) in Binney & Tremaine 2008):

$$\Phi_L(x, y) = \frac{1}{2} v_0^2 \ln\left(R_c^2 + x^2 + \frac{y^2}{q^2}\right) \quad (0 < q \leqslant 1). \quad (1)$$

Φ_L is stationary in a frame that rotates at angular speed Ω_b.

At $R = \sqrt{(x^2 + y^2/q^2)} \ll R_c$, Φ_L approximates the potential of the 2D harmonic oscillator. At $R \gg R_c$ and $q \simeq 1$, $\Phi_L \simeq v_0^2 \ln R$, which yields a nearly constant circular speed curve as observed in many disk galaxies.

The equipotentials of Φ_L have a constant axial ratio of q. The axial ratio $q_\rho \equiv b/a$ of the isodensity surfaces at a large radius is (Equation (2.72b) in Binney & Tremaine 2008):

$$q_\rho^2 \simeq q^4\left(2 - \frac{1}{q^2}\right) \quad (R \gg R_c). \quad (2)$$

In our standard model, we adopt $R_c = 0.1$, $q = 0.84$ (i.e., $q_\rho \simeq 0.54$ according to Equation (2)), $v_0 = 1$, and $\Omega_b = 1$. The units of length, velocity, and acceleration are arbitrary. These parameters place the bar corotation radius (CR) at $R_{CR} = 0.995$ (also the position for the L_1 and L_2 Lagrangian points). The Jacobi energy at R_{CR} is $E_{J,CR} = -0.495$.

We also tested other analytical and self-consistent N-body bar potentials and verified that our main conclusions remain unchanged.

For clarity and cleanness, in this paper we focus mainly on 2D planar orbits of test particles that are numerically integrated. The initial conditions of our test particles are randomly generated inside the equipotential surface to sample all possible orbital families, and the timestep is adaptively adjusted so that each orbit is integrated for about 800 azimuthal periods and each period is sampled by at least 512 points using a fourth-order Runge–Kutta integrator. The conservation of Jacobi energy E_J is generally better than 4×10^{-10} for 800 periods.

3. Results

Figure 1(a) shows the Poincaré SoS at $E_J = -1.08$ for our rotating barred potential. Each curve corresponds to an orbit with this E_J, and is the record of (y, v_y) whenever the orbit crosses the bar minor axis (y-axis) with $v_x < 0$ (to eliminate the sign ambiguity). Figure 1(a) shows two predominant regular orbital families within R_{CR}, namely the retrograde x_4 family (the left island of nested curves) and the prograde x_1 family (the right island). The center points of the two islands are the periodic x_4 and x_1 orbits, respectively. As discussed in the

Section 1, the fact that an orbit at a given energy is confined to a closed invariant curve indicates that this regular orbit admits an additional nonclassical IoM (I_2) at the given E_J. Thus, one may regard the invariant curves of regular orbits in the SoS as contour plots of I_2, where I_2 changes monotonically as regular orbits transition from one family to another.

Figure 1(b) shows the morphological transformation of the corresponding orbits in (a). The first orbit is a nearly periodic x_4 orbit corresponding to the center of the left island in Figure 1(a). As we move away from the periodic x_4 orbit, the enclosed area in the x_4 island in the SoS expands, the amplitude of the radial oscillations increases, and the orbits become thicker rosettes. When we leave the outskirt of the x_4 island and move into the x_1 orbital family, orbits become more box-shaped. Further along the sequence, orbits become more elongated in the direction of the bar major axis, and their enclosed area in SoS gradually shrinks to zero when reaching the periodic x_1 orbit, which is the last orbit in Figure 1(b) corresponding to the center of the right island in Figure 1(a). There is a continuous transition of orbital morphology, covering the entire phase space at the given E_J, from x_4 to x_1 families, which is accompanied by a monotonic change in I_2 respected by each regular orbit.

Searching for a proxy of I_2, we study orbits in the space of angular momentum (L_z) computed in the corotating reference frame of the bar. As expected, L_z is not a conserved quantity and is time-varying. Averaged over time, we can compute the mean angular momentum ($\overline{L_z}$) and the standard deviation (σ_{L_z}) of an orbit, where

$$\sigma_{L_z} \equiv \sqrt{\overline{[L_z(t) - \overline{L_z}]^2}}$$

reflects the amplitude of fluctuation over the duration of orbital integration. We have tested that halving or doubling the total time duration of the orbital integration changes the values of $\overline{L_z}$ and σ_{L_z} by only $\lesssim 1\%$ for regular orbits, but they do change by a larger fraction for chaotic orbits (see discussions regarding Figure 4).

Mapped into the angular momentum space of ($\overline{L_z}$, σ_{L_z}), the orbits with a given E_J follow a compact and nearly continuous sequence, and sequences of different energies are clearly separated in a nested layout (Figure 2). Even more strikingly, the sequence in Figure 2 directly and monotonically traces the nested invariant curves in the SoS and the continuous morphological transformation from the x_4 to x_1 orbits. Each sequence in the angular momentum space starts with a periodic x_4 orbit at the leftmost end and terminates at a periodic x_1 orbit at the rightmost end. Regular orbits connecting the periodic x_4 and the periodic x_1 in the SoS as illustrated in Figure 1 also keep their order in the angular momentum sequence. Such a monotonic mapping from the angular momentum sequence to invariant curves in the SoS indicates that these sequences do trace the monotonic change in I_2, hence it can serve as a proxy of I_2. The nested compact sequences also imply that both $\overline{L_z}$ and σ_{L_z} are nearly continuous functions of E_J and I_2.

We note that the location in a sequence in Figure 2, which follows I_2, can actually be uniquely and monotonically represented by the angle ϕ labeled in Figure 2. ϕ is equivalent to the CAM

$$\text{CAM} \equiv \overline{L_z}/\sigma_{L_z}$$

since $\cot\phi = -\overline{L_z}/\sigma_{L_z}$. The invariant curves in the SoS (Figure 1a) are also color coded with CAM. The smooth color
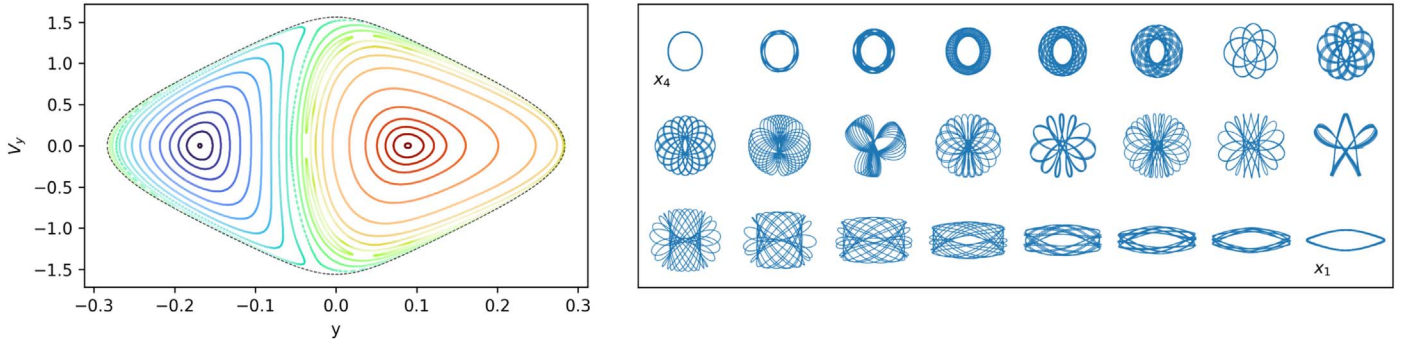
Figure 1. Left: (a) Poincaré SoS at $E_J = -1.08$ with the outmost dashed curve as the zero-velocity curve, i.e., the boundary of the energetically allowed region. Each closed curve corresponds to an orbit. Right: (b) the morphology transformation of the corresponding orbits in (a). The first x_4 orbit corresponds to the center of the left island in (a), then the orbits gradually transition to the last x_1 orbit corresponding to the center of the right island in (a). The invariant curves in (a) are also color coded with the CAM $\equiv \overline{L_z}/\sigma_{L_z} = -\cot\phi$ of the orbits. There is a continuous and smooth morphological transition from the periodic x_4 orbit to the periodic x_1 orbit, following the monotonic increase in CAM (or ϕ).
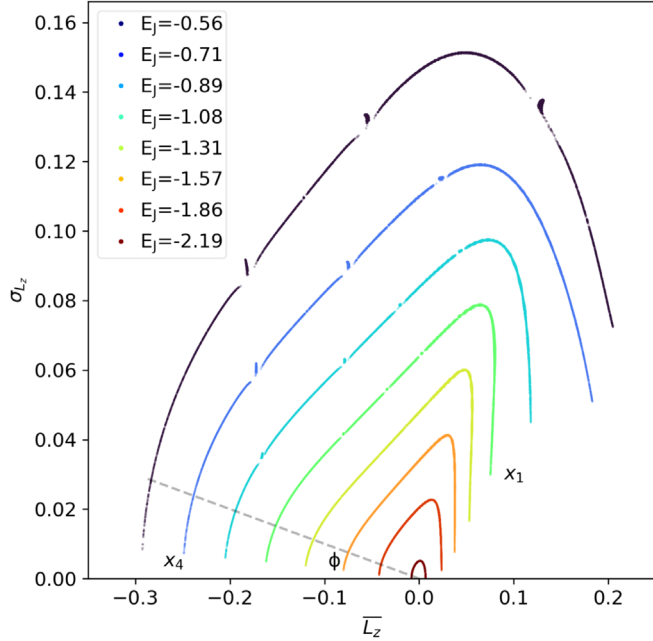

Figure 2. Orbital distribution in the angular momentum space ($\overline{L_z}, \sigma_{L_z}$) for our rotating barred potential. Colors indicate their energies (E_J). Note that the green curve ($E_J = -1.08$) corresponds to the orbits shown in Figure 1. An orbital sequence at a given E_J always starts from the periodic x_4 (the leftmost point) and ends at the periodic x_1 (the rightmost point).
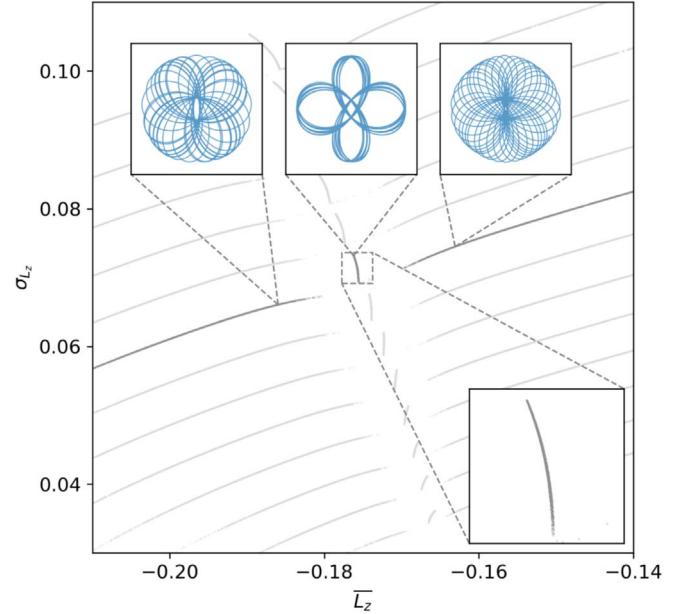

Figure 3. Zoom-in view of knots in the CAM sequence in Figure 2. The knot is produced by a 3:4 (azimuthal:radial) resonance (top middle inset). The weak chaos surrounding this resonance creates a discontinuity in the smooth distribution of $\overline{L_z}/\sigma_{L_z}$ across a wide range of energies (black points are for $E_J = -0.652$). The top left and top right insets show a smooth transition of orbital morphology near this resonance.

variation from the x_4 to x_1 families in the SoS again confirms that CAM indeed monotonically traces I_2 for regular orbits. Previous works used the average angular momentum to approximate I_2 in the vicinity of parent x_1/x_4 orbits (Binney & Tremaine 2008; Valluri et al. 2016). However, the monotonicity of $\overline{L_z}$ is not ensured; $\overline{L_z}$ increases in the x_4 branch, but may decrease slightly in the x_1 branch. We have verified that the nonmonotonicity of $\overline{L_z}$ is more pronounced in bars formed self-consistently from disk instabilities, such as the N-body bar model in Shen et al. (2010). Intriguingly, $\overline{L_z}$, after being normalized with σ_{L_z}, then becomes a monotonic and unique tracer of the entire phase space at a given E_J, smoothly connecting the x_1 and x_4 families into a single sequence.

Figure 2 also shows that the sequences in the angular momentum space have tiny breaks and knots for sufficiently high E_J. Figure 3 zooms in on one such break and knot region

with much longer orbital integration (around 6400 periods), and reveals that these features are associated with a high-order resonance. It is well known that stable high-order resonances can alter their local phase-space structure and induce chaos around them. Orbital morphology in the insets of Figure 3 clearly shows that the knot is actually a line segment due to a 3:4 (azimuthal:radial) resonance (lower inset of Figure 3), and the break around the knot may be related to the weakly chaotic orbits surrounding the resonance. The top tip of the line segment is a periodic 3:4 resonant orbit. Breaks and knots of a certain resonance are clearly aligned across different energies, carving out a valley across multiple sequences. Although high-order resonances and weak chaos appear as small localized breaks in the CAM sequence, they do not affect its global trend. In other words, the continuous sequence in the angular momentum space, also in CAM as the numeric proxy for I_2,

is insensitive to local, microscopic phase-space structures like high-order resonances.

The phase-space structure illustrated in Figure 1 is almost completely dominated by regular orbits of the x_1 and x_4 families, but a rotating barred potential may also have other major resonant families like x_2/x_3 and strong chaos around them. Thus, one may wonder if the CAM parameter is still an effective proxy of I_2 for regular orbits in the presence of strong chaos.

To study the phase space and the angular momentum space when x_2/x_3 families and strong chaos are present we reduce the pattern speed to $\Omega_b = 0.4$. Chaotic orbits have only one IoM and are not confined to orbital tori; they eventually fill the phase-space volume, bound by the nearby regular orbits of the same energy. Thus chaotic orbits will drift in the angular momentum space; their $\overline{L_z}$ and σ_{L_z} could change significantly after a long period of time. We may trace chaotic orbits using their drift in the angular momentum space. We cut the orbit into two equal halves and estimate their $(\overline{L_z}, \sigma_{L_z})$ separately. The differences between the two halves ($\Delta\overline{L_z}$ and $\Delta\sigma_{L_z}$) may be used to define the normalized drift:

$$\delta l = \sqrt{(\Delta\overline{L_z})^2 + (\Delta\sigma_{L_z})^2} \Big/ \sqrt{\overline{L_z}^2 + \sigma_{L_z}^2}.$$

The distribution of δl has a sharp break around 0.0224. Thus, we consider those orbits with $\delta l > 0.0224$ as possible chaotic orbits (painted gray in Figure 4). Note that δl is also reflected in the narrowness of the angular momentum sequence and the chaotic zone.

Figure 4 shows the $\overline{L_z}$–σ_{L_z} distribution of the orbits in the model with $\Omega_b = 0.4$. Short branches of the x_2 orbital family are clearly visible in the lower right corner of Figure 4. Similar to the sequences of the x_1 and x_4 families, periodic x_2 orbits are at the rightmost ends of these x_2 branches, and an x_2 orbit moves leftward along the sequence as it gradually deviates from the parent periodic x_2 orbit. The presence of an x_2 branch also induces a chaotic zone in the angular momentum space. Compared to the canonical case in Figure 2, the region near the maximum of σ_{L_z} on each sequence becomes diffuse, twisted, and dominated by strongly chaotic orbits.

The presence of the x_2 branch has complicated the phase-space structure. Unlike high-order resonances which only alter the local, microscopic phase-space structure, the presence of a strong resonance like x_2 can significantly reshape the phase space. Although parts of the x_1–x_4–x_2 sequence are interrupted by the presence of strong chaos, $\overline{L_z}/\sigma_{L_z}$ remains valid in tracing the local phase-space structure of all stable islands of the x_1, x_4, and x_2 families. Since the angular momentum space is presumably a projection of the E_J–I_2 space, it is not surprising that chaotic orbits, which do not respect I_2, are detached from the sequences of regular orbits. Instead, they become clouds of scattered points in the angular momentum space (gray points in Figure 4). Weakly chaotic orbits diffuse slower, thus they may still remain close to the angular momentum sequence. Surprisingly and fortunately, even chaotic orbits roughly follow the CAM sequence and do not affect much its monotonicity, except for the strongly chaotic zone at the upper tip of the x_1 branch, where the monotonicity fails locally.
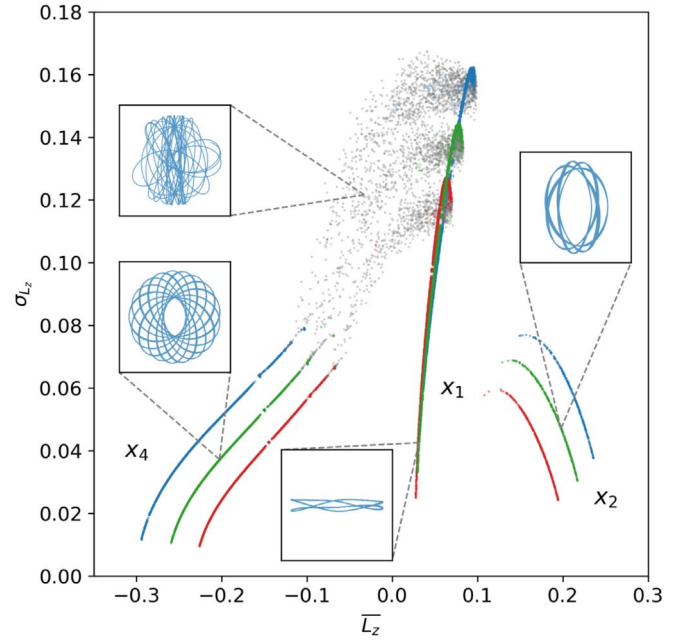

Figure 4. Phase-space structure for the model with x_2 orbits for $E_J = -0.57$, -0.68, and -0.80 (blue, green, and red, respectively). Note that the potential's long axis is horizontal. Compared to the canonical case shown in Figure 2, there is a strong, prograde (positive $\overline{L_z}$) x_2 subsequence. There is no subsequence for the x_3 orbital family since it is unstable. Between the sequences of the x_1 and x_4 orbits, there is a diffuse zone of strongly chaotic orbits (gray colored for those with $\delta l > 0.0224$). The orbits are integrated for 3200 azimuthal periods. Typical orbits from each regular orbital family and the chaotic zone are illustrated in insets.

4. Discussions

4.1. Asymptotic Behaviors in Limiting Cases

CAM remains a well-behaved proxy of I_2 in most limiting cases as we discuss below. A nonrotating bar, like a stationary tri-axial potential, is dominated by box orbits and loop orbits (Binney & Tremaine 2008). Box orbits (like Lissajous figures) have zero net angular momentum while loop orbits have nonzero net angular momentum. As Ω_b gradually approaches zero, x_4/x_2 orbits in rotating barred potentials become retrograde/prograde loop orbits, and x_1 orbits become box orbits with $\overline{L_z} = 0$ (Valluri et al. 2016). For the loop orbits, $|\overline{L_z}|$ and σ_{L_z} form an anticorrelated sequence at a given energy (due to the trade-off between rotation and random motions), thus $\overline{L_z}$ is the most obvious proxy of I_2. However, CAM, in addition to $\overline{L_z}$, still remains a good proxy of I_2. Also, the interconnection of boxy/loop orbits to the $x_1/x_4/x_2$ orbits again reveals the continuity of orbital families in the phase space (Binney & Spergel 1984).

As q in Equation (1) approaches unity, we get an axisymmetric disk which supports only loop orbits with the canonical momentum $p_\phi = L_z$ being an exact IoM and $\sigma_{L_z} = 0$. When the axisymmetric disk is viewed in a rotating frame with angular speed Ω_b, the angular momentum in the corotating frame, $L_z = p_\phi - \Omega_b R^2$, is no longer an integral. The CAM sequence of loop orbits (corresponding to x_4 and x_1 in a rotating barred potential) becomes a distorted arch in angular momentum space; the prograde side of the arch is distorted toward $\overline{L_z} = 0$ and vice versa for the retrograde side. This is similar to the case in Figure 2, where the x_1 branch is closer to

$\overline{L_z} = 0$ than the x_4 branch. Again, CAM, in addition to $\overline{L_z}$, is still a good proxy of I_2 in the axisymmetric case despite the fact that L_z (unlike p_ϕ) is not an integral.

4.2. Advantages and Potential Applications

CAM is a good proxy of I_2 even in the presence of high-order resonances and chaotic orbits. CAM fixes the issue of nonmonotonicity of $\overline{L_z}$ in tracing the orbital families by taking into account the amplitude of fluctuation in the time-varying L_z (σ_{L_z}), which contains valuable information but was previously underappreciated. CAM is also independent of the Hamiltonian of the system (E_J), and can serve as a good diagnostic of dynamical systems.

We have verified that it is well behaved in generic rotating bar or tri-axial potentials, including a self-consistent N-body bar model designed to match the Milky Way boxy bar/bulge (Shen et al. 2010). It may be generalized to other Hamiltonian systems—any Hamiltonian that has position-like and momentum-like variables, from which we could construct angular momentum–like variables.

There are many potential applications of the empirical proxy. An immediate application of CAM is accurate and quick orbital classification in a barred potential without knowing the detailed properties of the orbital families. This is particularly useful for 3D orbits whose phase space cannot be easily visualized. The CAM orbital classification method is complementary to frequency-based classification methods (Binney & Spergel 1982; Valluri & Merritt 1998). Note that neither irreducible frequency components nor frequency ratios are proper substitutions of IoMs. As a proxy for I_2, CAM is more directly related to the fundamentals of orbits. There are less degeneracies associated with CAM (I_2) than frequency-based methods since orbits with the same frequency ratio can be distinguished by their intrinsic differences in E_J and I_2. For example, one can easily distinguish x_1 and x_2 orbits with CAM whereas additional constraints are required to separate them in frequency-based methods (e.g., Valluri & Merritt 1998; Valluri et al. 2016). The computation of CAM is also computationally less expensive than the Numerical Analysis of Fundamental Frequencies (NAFF) method (Laskar 1993). We have successfully applied it to classify real orbits in N-body simulations of barred galaxies, and the results will be presented in a follow-up paper.

4.3. Limitations

CAM is only an empirical proxy of the analytically unknown I_2. Numerical integration over a sufficient number of periods with a priori knowledge of the potential is required to accurately compute CAM. In contrast, a genuine IoM is only a function of phase-space coordinates at any moment. It is also important to keep in mind that CAM may not be the only proxy of I_2 for a given barred potential. Several other methods have been developed to estimate or approximate IoMs, particularly action variables, for numerically integrated orbits in generic tri-axial or axisymmetric potentials (Sanders & Binney 2014, 2016).

5. Summary

We discover a good proxy for the second IoM I_2 in rotating barred or tri-axial models, namely CAM $\equiv \overline{L_z}/\sigma_{L_z}$, which monotonically traces various orbital families at a given energy

in a rotating barred potential even in the presence of resonant and chaotic orbits. This empirical proxy of I_2 may be used to parameterize pseudo DFs in the construction of dynamical models, such as Schwarzschild (Schwarzschild 1979) or made-to-measure models (Syer & Tremaine 1996), for real-world observations of rotating barred or tri-axial galaxies. However, we need a priori information about the potential to carry out the calculation. Also, CAM-based pseudo DFs do not measure the true phase-space density, as CAM is only a dimensionless numerical proxy.

Despite its effectiveness, we still do not fully understand why CAM is such a good proxy of I_2. Further study is needed to better understand this relationship. Investigation in the framework of Hamiltonian perturbation theory, and focus on more complicated orbital cases (e.g., real 3D orbits in an N-body simulation), could be illuminating.

ORCID iDs

Yu-Jing Qin ⓘ https://orcid.org/0000-0003-3658-6026
Juntai Shen ⓘ https://orcid.org/0000-0001-5604-1643

References

Binney, J., Gerhard, O. E., & Hut, P. 1985, MNRAS, 215, 59
Binney, J., Gerhard, O. E., Stark, A. A., Bally, J., & Uchida, K. I. 1991, MNRAS, 252, 210
Binney, J., & Spergel, D. 1982, ApJ, 252, 308
Binney, J., & Spergel, D. 1984, MNRAS, 206, 159
Binney, J., & Tremaine, S. 2008, Galactic Dynamics (2nd ed.; Princeton, NJ: Princeton Univ. Press)
Blitz, L., & Spergel, D. N. 1991, ApJ, 379, 631
Contopoulos, G., & Grosbol, P. 1989, A&ARv, 1, 261
Henon, M., & Heiles, C. 1964, AJ, 69, 73
Laskar, J. 1993, CeMDA, 56, 191
Lynden-Bell, D. 1962, MNRAS, 124, 1
Masters, K. L., Nichol, R. C., Hoyle, B., et al. 2011, MNRAS, 411, 2026
Menéndez-Delmestre, K., Sheth, K., Schinnerer, E., Jarrett, T. H., & Scoville, N. Z. 2007, ApJ, 657, 790
Patsis, P. A., Skokos, C., & Athanassoula, E. 2002, MNRAS, 337, 578
Sanders, J. L., & Binney, J. 2014, MNRAS, 441, 3284
Sanders, J. L., & Binney, J. 2016, MNRAS, 457, 2107
Schwarzschild, M. 1979, ApJ, 232, 236
Sellwood, J. A., & Wilkinson, A. 1993, RPPh, 56, 173
Shen, J., Rich, R. M., Kormendy, J., et al. 2010, ApJL, 720, L72
Skokos, C., Patsis, P. A., & Athanassoula, E. 2002, MNRAS, 333, 847
Syer, D., & Tremaine, S. 1996, MNRAS, 282, 223
Valluri, M., & Merritt, D. 1998, ApJ, 506, 686
Valluri, M., Shen, J., Abbott, C., & Debattista, V. P. 2016, ApJ, 818, 141
Xia, T. Y., & Shen, J. 2021, ApJ, submitted